Materials & Design 233 (2023) 112207

Contents lists available at ScienceDirect

Materials & Design

journal homepage: www.elsevier.com/locate/matdes

Auxetic response of additive manufactured cubic chiral lattices at large plastic strains

Caterina Iantaffi [a,b,*], Eral Bele [a,*], David McArthur [a,b], Peter D. Lee [a,b], Chu Lun Alex Leung [a,b,*]

[a] Mechanical Engineering, University College London, Torrington Place, London WC1E 7JE, UK
[b] Research Complex at Harwell, Rutherford Appleton Laboratory, Oxfordshire OX11 0FA, UK

ARTICLE INFO

Keywords:
Auxetic lattices
Chiral lattices
Additive manufacturing
X-ray computed tomography
FEA

ABSTRACT

Auxetic lattices exhibit a negative Poisson's ratio and excellent energy absorption capability. Here, we investigate the compressive performance of auxetic cubic chiral structures. By utilising finite element analysis (FEA) verified by interrupted mechanical testing and x-ray computed tomography, the auxeticity and failure mechanisms at the large strain deformation have been evaluated. The FEA results show that the initial elastic–plastic response agrees with the prediction of the classic scaling laws of bending-dominated lattices. At increasing plastic deformation, the energy absorption and auxeticity are dependent on relative density, *i.e.,* the slenderness ratio, of the constitutive struts. In the plastic regime, the auxeticity decreases with relative density. Ductile fracture precedes densification in relative densities above 1.2%, thus dictating a new scaling law for the variation of the maximum energy absorbed with density. The numerical model predicts the scaling of mechanical properties, fracture strains, and energy absorption of the constitutive unit cell and finite-sized specimens in the relative density ranging from 0.3% to6.5%. However, to accurately model the failure mechanism, geometrical imperfections should be included. The scaling laws derived from this work may aid the design of next generation auxetic lattices with tailored mechanical properties.

1. Introduction

Additive manufacturing (AM) technologies produce parts with unparalleled levels of design flexibility and excellent mechanical properties compared to those made by traditional manufacturing methods [1]. Further to materials and process developments, AM research is shifting towards the design and manufacturing of lightweight complex structures.

One such class of structures is auxetic micro-lattices, periodic architectures that exhibit negative Poisson's ratio (NPR), *i.e.,* the structure expands under tensile load, and it contracts under compression. According to the classical elasticity theory, the material's Poisson's ratio plays a crucial role in determining numerous mechanical properties. Auxetic structures exhibit exceptional mechanical characteristics, including enhanced shear modulus, superior energy absorption capacity, increased fracture toughness, and improved wear resistance [2]. They have attracted attention in various fields, including biomedical [3], space [4], aerospace [5], and acoustic applications [6].

The auxeticity is dictated by the lattice topology and is activated by three main deformation mechanisms: (i) rotating rigid, (ii) re-entrant and (iii) chiral [7]. AM technologies have enabled novel designs for 2D and 3D auxetic topologies, *e.g.,* triply-periodic core/shell cubic crystals [8], re-entrant geometries [9,10], sliding-based mechanisms [11,12], and chiral lattices [14,15,17]. Auxetic chiral lattices exhibit a negative Poisson's ratio value up to −1 [15]. Nevertheless, few studies have focused on the large plastic deformation response [16], despite its importance in the auxeticity evolution, energy absorption capabilities, and shape recovery properties [18,19]. At large strains, the mechanical behaviour of a lattice may undergo nonlinear deformation behaviour (*e.g.,* buckling), localised deformation (*e.g.*, shear bands), and fracture, therefore, the materials properties defined by classic elasticity and plasticity models may be not accurate. The lattice topology, *e.g.,* stretch-dominated or bending-dominated, and the relative density, affect the failure modes and the transition from linear elastic to non-linear inelastic response [20].

There are two other crucial factors that influence the mechanical behaviour and must be considered to ensure the accurate numerical analysis of the response of auxetic lattices at large strains. Firstly, the size of the model geometry needs to be large enough to reproduce the macroscale effective response of the lattice, *i.e.,* when the edge effects

* Corresponding authors at: Mechanical Engineering, University College London, Torrington Place, London WC1E 7JE, UK (C. Iantaffi, E. Bele and C.L.A. Leung).
E-mail addresses: caterina.iantaffi.19@ucl.ac.uk (C. Iantaffi), e.bele@ucl.ac.uk (E. Bele), alex.leung@ucl.ac.uk (C.L.A. Leung).

https://doi.org/10.1016/j.matdes.2023.112207
Received 11 May 2023; Received in revised form 26 July 2023; Accepted 30 July 2023
Available online 4 August 2023

stop influencing the deformation mechanisms [21]. Smaller specimens have lower elastic modulus due to higher stress concentrations per volume near sample boundaries [22]. Morrish [23] found that a minimum of four-unit cells is necessary to test size-independent elastic–plastic mechanical properties of Ti6Al4V electron beam powder bed fusion (EPBF) diamond lattice structures. Due to the potential impact of topology on the overall mechanical performance, more mechanical testing may be required to validate the minimum geometric size to accurately mimic the effective response of the auxetic lattices.

Secondly, the mechanical performance of lattices is influenced by the presence of the AM defects, *e.g.* porosity [24–26] and dimensional inaccuracies, such as surface texture or roughness due to the powder sintering during preheating [27] and fluctuations in printing conditions [28]. The powder sintering causes volume oversizing and change of strut cross-section from circular to ellipsoid shape [29,30], especially in horizontal [31] and inclined struts (*i.e.* staircase effect [32]) and at nodes [33]. Internal porosities can have a detrimental effect on tensile properties, inducing stress concentration and premature yield.

The as-built lattice structure is far from a defect-free model with idealised geometry [33–35]. Finite element analysis (FEA) models based on x-ray computed tomography (XCT) analysis can help avoid erroneous approximation of the lattices' mechanical performance. XCT can also be used to visualise and quantify the lattice defects [36] and generate a more accurate 3D finite element model [37]. *In situ* mechanical testing with XCT can be used to monitor damage evolution, determine the lattice weak spots, and determine the influence of defects on the failure mechanisms [38,39].

Here, we investigate the compressive response of EPBF Ti-6Al-4V eigenmode 10 cubic chiral lattice [14] by FEA and interrupted mechanical compression testing with XCT. This lattice exhibits full auxetic behaviour and the ability to form synclastic (dome-shaped) curvatures under out-of-plane bending stress, making it ideal for curved parts, *e.g.,* tracheal stent [3], aircraft wing panel and nose cone [40]. The high energy absorption capacity makes it ideal for crash and blast protection parts [40,41]. Despite their potential for numerous engineering applications, these lattice architectures have received limited attention. Based on previous linear numerical analysis, the cubic chiral lattice structure exhibits auxeticity in the elastic regime, with an isotropic Poisson's ratio of −0.4 [14] controllable by tuning geometrical parameters such as amplitude; at increasing amplitude, the auxeticity reduces [43]. However, it is unclear how the auxetic response evolves in the plastic regime, or how it scales with relative density. The experimental validation of the elastoplastic, auxetic, and large-strain deformation mechanisms is limited.

Warmuth [44] numerically and experimentally studied the compressive properties of cubic chiral lattices and the influence of the geometrical parameters, such as strut thickness and amplitude. Increasing the amplitude modifies the deformation from buckling to bending-dominated. A Poisson's ratio of −0.2 is measured in the elastic domain, however it differs from numerical prediction due to AM inaccuracies. Novak [43] demonstrated the excellent impact absorption capabilities. Although there was good agreement with the experimental results at low strain rates, beam elements are not ideal for simulating twisting and bending mechanisms at large strain failure regimes and in struts with lower aspect ratios [45]. Nodes are considered the weakest point with the larger stress concentrations [43] and manufacturing defects density. This implies that making topological modifications, *e.g.,* varying the strut thickness along their length and joining to improve bending, has the potential to enhance the energy absorption capacity of chiral lattices. Du Plessis [46] reported that the largest deformation occurs at the nodes of very thin struts. However, in other typical porous structures, failure tends to occur after yielding on tension-loaded horizontal struts because of the high-stress concentration induced by printing inaccuracies [38]. In summary, the initiation and propagation of failure mechanisms of this lattice at a range of relative densities and large strains are still not well understood [44].

In this study, numerical models on a representative unit cell (*i.e.,* an infinite lattice), and a finite-sized geometry are performed to determine (i) the scaling of the elastoplastic properties and auxeticity with relative density, (ii) the initiation and propagation of ductile failure, and (iii) the evolution of auxeticity with plastic strains. The experimental results from *in situ* interrupted compression testing with XCT supported the quantification of the effects of manufacturing inaccuracies on deformation mechanisms. This detailed information could inspire the next-generation design of auxetic lattice architectures with tailored mechanical properties.

2. Methods

2.1. Numerical models

The effective compressive response of the cubic chiral lattice was investigated using FEA. Five lattice geometries with relative density ranging from 0.3% to 6.5%, have been designed by changing the strut thickness. From the numerical stress–strain response, the characteristic scaling relationships for stiffness and yield strain with density have been defined. The evolution of Poisson's ratio with principal strain has been analysed to assess the auxetic behaviour in the elastic–plastic regime and its dependence on relative density. The numerical analysis has been conducted both on the infinite lattice geometry (*i.e.,* examining the effective properties), and an exemplary finite-sized specimen geometry, to assess whether the mechanical performance is size-dependent. Fig. 1 shows the geometry of these two main models: (i) a representative volume element (RVE) consisting of the constitutive unit cell (Fig. 1a), and (ii) a finite-sized geometry (Fig. 1b) that replicates the experimental specimen. The unit cell is a cubic quadratic geometry (eigenmode 10 [14]) with a nodal distance $n = 3$ mm and an amplitude$m = 0.6$ mm, see Fig. 1a. The strut thickness, t, was in the range $0.1 \le t \le 0.5$ mm, providing relative densities, ρ^*/ρ_S, in the range $0.3\% \le \rho^*/\rho_S \le 6.5\%$, where ρ^* and ρ_S denote the densities of the lattice and solid material, respectively. The finite-size specimen is an arrangement of $2 \times 2 \times 3$ units cells, with dimensions $12 \times 12 \times 18$ mm, see Fig. 1b.

The constitutive material was modelled with the bulk properties of EPBF Ti6Al4V, with Young's modulus $E = 115$ GPa, isotropic Poisson's ratio $\nu = 0.29$, and isotropic hardening defined by the Johnson-Cook strain rate-independent plasticity model [47]:

$$\sigma^0 = \left[A + B\left(\bar{\varepsilon}^{pl}\right)^n\right]\left(1 - \widehat{\theta}^m\right) \tag{1}$$

where σ^0 is the plastic flow stress, $\bar{\varepsilon}^{pl}$ is the equivalent plastic strain, $\widehat{\theta}$ is the non-dimensional temperature, and $A, B, n,$ and m are the material properties reported in ref [48], see Table 1.

The fractographs showed that the failure of the AM sample was primarily ductile under uniaxial compression, see Supplementary Fig. 2. In the FE models, the ductile damage initiation was defined by the Johnson-Cook (JC) criterion [49]:

$$\bar{\varepsilon}_D^{pl} = \left[\mathrm{D}_1 + \mathrm{D}_2 exp(-\mathrm{D}_3\eta)\right]\left[1 + \mathrm{D}_4 ln\left(\frac{\dot{\bar{\varepsilon}}^{pl}}{\dot{\varepsilon}_0}\right)\right](1 - \mathrm{D}_5\widehat{\theta}) \tag{2}$$

where $\bar{\varepsilon}_D^{pl}$ is the equivalent plastic strain at the onset of damage, η is the stress triaxiality, $\dot{\bar{\varepsilon}}^{pl}$ and $\dot{\varepsilon}_0$ are the equivalent plastic and reference strain rates, respectively, and D_1-D_5 are damage parameters [49]. Here, we consider the static response without temperature dependence, thus $\mathrm{D}_4 = \mathrm{D}_5 = 0$; see key parameters in Table 1. Damage propagation was specified through a linear damage evolution, with fracture energy per unit area obtained from the uniaxial stress–strain curve [48] as $G_f = \int_{\bar{\varepsilon}_0^{pl}}^{\bar{\varepsilon}_f^{pl}} L\sigma_0 d\bar{\varepsilon}^{pl}$, where L is the characteristic element length, and $\bar{\varepsilon}_0^{pl}$ and $\bar{\varepsilon}_f^{pl}$ are the equivalent plastic strain at the onset of damage and complete failure,

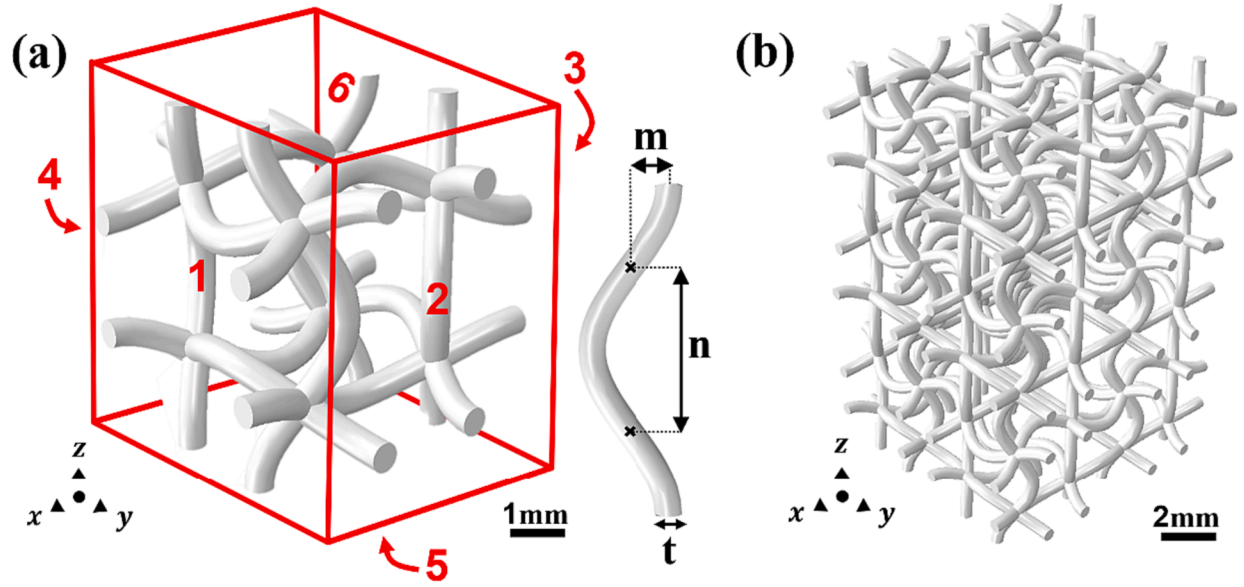

Fig. 1. 3D FEA model geometries representing, (a) the cubic chiral lattice unit cell with the 6 faces for PBCs, with an enlarged view of a strut with definition of nodes distance (n), amplitude (m), and thickness (t), and (b) the finite-sized specimen made of 2x2x3 unit cells.

Table 1
Material properties of Ti6Al4V [48].

Property	Value	Unit
Elastic modulus	115,000	MPa
Poisson's ratio	0.29	–
JC hardening model	$A = 429.0$	MPa
	$B = 1428.0$	MPa
	$n = 0.34$	
JC damage model	$D_1 = -0.09$	-
	$D_2 = 0.25$	-
	$D_3 = 0.5$	-
Fracture Energy	0.208	mJ/mm^2
Mass density	4.4	g/cm^3
Coefficient of friction (self)	0.3	–
Coefficient of friction (plates)	0.4	–

respectively.

To model the effective response of the lattice via the unit-cell RVE, periodic boundary conditions (PBCs) corresponding to cubic symmetry were imposed by coupling the corresponding nodes of parallel faces of the RVE [50]:

$$\begin{aligned} u_i^1 - u_i^3 &= 2N\varepsilon_{i1}^{\infty} \\ u_i^2 - u_i^4 &= 2N\varepsilon_{i2}^{\infty} \\ u_i^6 - u_i^5 &= 2N\varepsilon_{i3}^{\infty} \end{aligned} \tag{3}$$

where $i = 1, 2, 3$ correspond to the x, y, z principal directions, respectively, u_i^1 refers to the nodal displacement on face 1 in direction i, and $\varepsilon_{i1}^{\infty}$ is the remote strain in the $i1$-direction, see Fig. 1a. The uniaxial compressive response in all three principal directions was investigated by imposing a remote displacement on the corresponding nodes, while the response of the finite-sized specimens was simulated by compressing the model through two analytical rigid surfaces. To capture the effect of densification at large strains, self-contact was defined between all surfaces, through a penalty definition with a coefficient of friction $\mu = 0.3$. The contact properties between the rigid plates and the lattice were imposed with a coefficient of friction $\mu = 0.4$, which is representative of the static friction of titanium on steel [51].

The models were meshed with linear tetrahedral elements with a minimum of 6 elements/diameter. The FEA was conducted with the explicit solver of the commercial package Abaqus 2017. In all analyses, the remote strain rate was kept between 0.08 and 0.2 s^{-1}, producing a sufficiently small kinetic/internal energy ratio of $\sim<10^{-3}$ to replicate the quasi-static compression.

2.2. Specimen manufacturing

The specimens were manufactured with an Arcam Q10 EPBF machine using gas atomized Ti–6Al–4V powder in the range of 45 - 105 μm. The EPBF system was operated within a 3×10^{-3} mbar vacuum with regulated helium, 50 μm layer thickness, constant voltage (U) of 60 kV, electron beam current (I) of 1.5 mA and scanning speed (v) of 180 mm/s, resulting in a line energy (E) of 0.5 J/mm ($E = U \bullet \frac{I}{v}$).

By analysing the reconstructed XCT data of the printed sample, the node distance and the amplitude were quantified to define the unit cell geometry for the numerical models. The volume rendering of the printed lattice is shown in Fig. 2a. Significant variation in the strut cross-sectional areas is observed and further analysed. Fig. 2b-d show the thickness distribution in a selected unit cell with an average strut thickness of 490 ± 110 μm. A low 0.12% volume of internal porosity has been quantified and examples of pore distribution in a vertical strut, a horizontal strut and at struts intersection (*i.e.,* node), are shown in Fig. 2e.

2.3. In situ compression tests with x-ray computed tomography (XCT)

Prior to compression, tomographic scans were performed on the undeformed specimen. Two types of scans were performed using a Nikon Metris 225 XCT system using reflection anode: (i) the lattice was scanned at 125 kV and 150 μA, comprising of 4476 projections, with a 354 ms exposure time per projection and a voxel size of $7.9 \times 7.9 \times 7.9$ μm^3; (ii) a high-resolution scan of the unit cell was scanned at 110 kV and 81 μA, comprising of 4476 projections with a 708 ms exposure time per projection, and a pixel size of $2.5 \times 2.5 \times 2.5$ μm^3. We used 64 flat and dark images prior XCT scans acquisition. The reconstruction, data analysis and interpretation follow the standard practice of pore size quantification depicted in ref. [52,53].

A Deben CT5000 compression rig with a 5 kN load cell was integrated into the XCT system. The sample was loaded into the rig and its top and bottom were sandwiched between steel plates, respectively. A displacement-controlled compression test was conducted at a constant displacement rate of 1 mm/min (strain rate 10^{-4} s^{-1}), continuing until

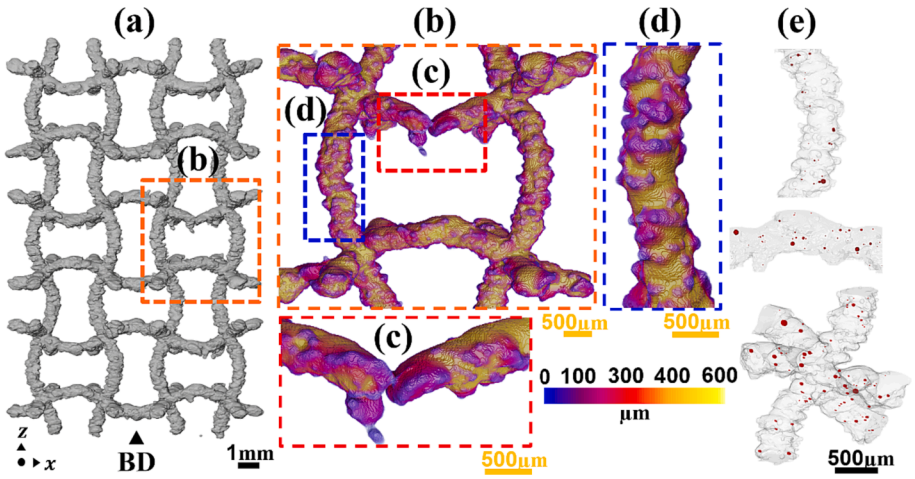

Fig. 2. X-Ray CT volume rendering of (a) the manufactured lattice sample from $x-y$ plane view; (b) the unit cell with local thickness coloured map with highlighted (c) a horizontal and (d) vertical strut; (e) a vertical, horizontal strut and a node with (red) highlighted internal pores. (For interpretation of the references to colour in this figure legend, the reader is referred to the web version of this article.)

complete structural failure. The loading direction was parallel to the sample's build direction (z axis in Fig. 2a). For every 0.1 strain increment, the compression test was interrupted, and the strain was held constant while the XCT scan was performed.

The data was reconstructed using the embedded cone beam filtered back projection algorithms in CT Pro Nikon. The image analysis was performed using Avizo 9.3 (ThermoFisher). We visualised and quantified internal defects and deformation mechanisms throughout compression, see quantification details in ref [27]. The local strut thickness analysis was performed using the Fiji plugin BoneJ [54], see Supplementary Fig. 1.

3. Results

3.1. Compressive response of the chiral lattice RVE

The uniaxial compressive response of the cubic chiral lattice RVE in the density range $0.3\% \leq \rho^*/\rho_S \leq 6.5\%$ is shown in Fig. 3a. The response indicates that the unit cell exhibits bending-dominated deformation, demonstrating a linear regime, followed by plateau stress, and densification. The equivalent stress distribution during these deformation regimes is reported in Fig. 3b-d for the RVE with a relative density of $\rho^*/\rho_S = 6.5\%$.

In the linear regime, the equivalent stress is primarily in the elastic range, with an incipient zone of plastic stress located in the tensile and compressive surfaces of the struts, see Fig. 3b. Then, a plastic hinge develops at the mid-length of the strut aligned with the loading direction and expands throughout the length resulting in the plateau region of the stress–strain curve, see Fig. 3c and inset. Finally, the densification occurs as struts contact each other, see Fig. 3d and inset. The densification strain increases at low relative densities, *e.g.,* 0.35 strain for a relative density $\rho^*/\rho_S = 1.2\%$, because the inter-struts contact occurs at larger strains. An identical stress–strain response was found in the other two compression directions indicating an isotropic response, see Supplementary Fig. 2.

The chirality of the unit cell promotes an inward nodal displacement during compression, giving rise to the auxetic behaviour. Poisson's ratio is defined as $\nu_{ij} = -\varepsilon_{jj}/\varepsilon_{ii}$, where ε_{ii} is the applied strain and ε_{jj} the

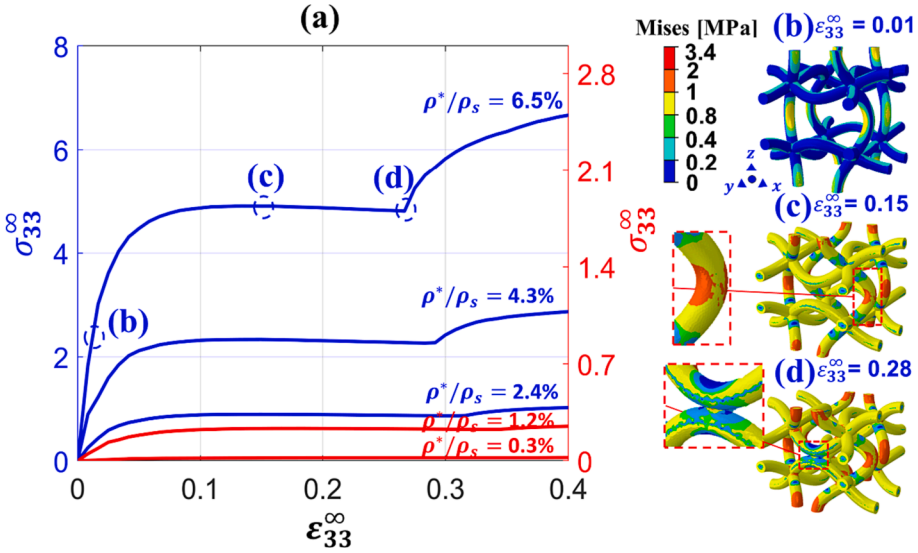

Fig. 3. Numerical compressive stress–strain response of (a) the cubic chiral lattice RVE in the relative density range $0.3\% \leq \rho^*/\rho_S \leq 6.5\%$; 3D rendered von Mises stress distributions of the RVE with $\rho^*/\rho_S = 6.5\%$ in (b) the elastic; (c) the plateau and; (d) the densification regimes. The corresponding insets illustrate in (c) the plastic hinge development and (d) densification.

transverse strain. For the unit cell with a relative density $\rho^*/\rho_S = 6.5\%$, the evolution of Poisson's ratios with principal strains is shown in Fig. 4.

In the linear regime, the auxetic response is isotropic, with $\nu_{ij} \sim -0.32$, whereas in the plastic (plateau) regime two distinct responses are observed. The unit cell contracts preferentially in one direction, developing two groups: $\nu_{31} = \nu_{12} = \nu_{23}$ and $\nu_{21} = \nu_{32} = \nu_{13}$. This results in a negative Poisson's ratio of larger magnitude in the preferred contraction direction ($\nu_{21} = \nu_{32} = \nu_{13}$), and a larger difference between the two groups of ν_{ij} at increasing principal strain. Densification occurs due to the contact between struts aligned with the axis of preferred contraction as illustrated by the insets in Fig. 3d.

The effect of ductile damage on the compressive response of unit cells with relative densities $\rho^*/\rho_S = 6.5\%$ and $\rho^*/\rho_S = 1.2\%$, is shown in Fig. 5a-b, respectively. In RVE with a relative density $\rho^*/\rho_S \geq 2.4$, the initiation and propagation of ductile damage occurs in the plateau regime. The distribution of the Johnson-Cook damage initiation criterion (JCCRT in Abaqus) is shown in Fig. 5b. The criterion of *Equation (2)* is met when JCCRT = 1 in the plastic hinge of struts aligned with the loading direction. Propagation of ductile damage occurs in both inward and outward surfaces of the plastic hinge (inset in Fig. 3c) and is quantified by the stiffness degradation parameter, SDEG. Element removal occurs when SDEG = 1 in the integration point, shown in Fig. 5c. The latter leads to the softening behaviour of the unit cell. For struts with a higher slenderness ratio (*e.g.*, in unit cells with $\rho^*/\rho_S \leq 1.2\%$), the damage does not occur until after densification. The initiation of the damage is mainly located in the plastic hinges of struts aligned with the loading direction. The damage propagation occurs in the nodes that are closer to the periodic boundaries Fig. 5e-f. Up to the propagation of damage, these locations have an identical stress state to those located at mid-strut.

The lattice fracture strain increases with decreasing relative density, from $\varepsilon_{33}^{\infty} = 0.13$ ($\rho^*/\rho_S = 6.5\%$) to $\varepsilon_{33}^{\infty} = 0.36$ ($\rho^*/\rho_S = 1.2\%$), *i.e.,* this improves the energy absorption capabilities. For $\rho^*/\rho_S = 0.3\%$, there is no ductile failure activation due to the increased slenderness ratio. This is further analysed in the Discussion section below.

3.2. Compressive response of finite-sized lattices

The numerical compressive response, with and without activated damage criteria, of finite-sized lattice specimens is shown in Fig. 6a. In the absence of ductile failure, the elastoplastic response in the initial two stages of compression (linear and plateau) is similar to the unit cell response, however at this strain range, the finite-sized specimens do not exhibit the rapid increase in stress associated with the densification regime. Fig. 6b-d report the relevant deformation mechanisms in the 3D rendered von Mises stress distributions. Failure predominantly initiates in the mid-length plastic hinge regions of vertical and horizontal struts, see Fig. 6b. At regimes with increasing strain deformation, a distinct shear band forms in the $x-y$ plane at 45° to the loading direction which results in the plateau regime, see Fig. 6c. Localised deformation within this band is indicative of the surface constraints of the plate/specimen boundary; a similar deformation behaviour has been observed by Warmuth [44]. In the plateau regime, the localised deformation in the struts proceeds at the boundaries of the shear band, indicated by high stress concentration in the plastic hinges, see Fig. 6c-d.

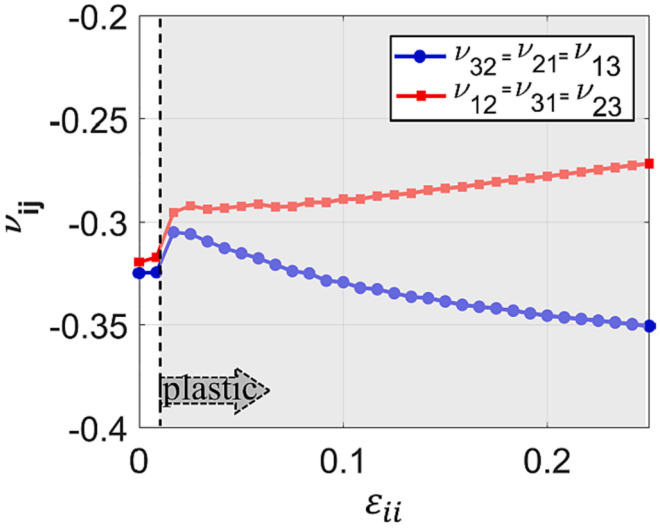

Fig. 4. Poisson's ratios for *x*, *y* and *z* directions dependency with compression strain at a relative density of 6.5%.

Unlike the RVE in Fig. 3, the finite-sized lattice exhibits non-uniform deformation and gradual stress–strain curve increase due to sliding contact of struts, which is enabled by the plate/specimen and the specimen free boundaries. The implication of this response is that the energy/unit volume absorption capacity of the finite-sized lattice (typically in the strain range of the plateau stress), may be larger than the corresponding RVE lattice. In practice, the absorption capacity will be lower than the theoretical values due to fracture.

The compressive response of the experimental specimen is also reported in Fig. 6a. The relative density quantified from the XCT scans is $\rho^*/\rho_S = 6.79\%$, with a calculated mean strut diameter of $d = 490 \pm 100\mu m$. There is a relatively good agreement in the initial elastoplastic response between the experimental specimen and the numerical model with the closest relative density, see Discussion below. Likewise, the deformation mechanisms, shown in Fig. 6e-g, present good agreement with the numerical prediction, showing the development and evolution of a distinctive shear band during the plateau regime. The elastic stiffness and yield strength are reported in detail in the discussion section.

In the numerical models, ductile fracture is initiated in the vertical struts that are closest to the plates, which are comparatively more confined to lateral displacements, see failure locations in Fig. 6b. Numerical instabilities are encountered after complete stiffness degradation (*i.e.,* removal) of all elements in the thickness of vertical struts; therefore, the model is limited to predicting the first complete fracture. In the experimental specimen, the fracture evolution is gradual, occurring first at horizontal struts with large geometrical imperfections and spreading gradually to other struts; the failure locations are shown in Fig. 6e-f.

To understand whether internal defects and geometrical imperfections influence the failure mechanisms of the lattice structure, local struts thickness and porosity have been quantified using XCT and image analysis. The mean pore diameter is found to be less than 10 μm, see Fig. 2e. The largest concentration of porosity is at the nodes (0.16% volume fraction), followed by the horizonal and vertical struts (0.11% and 0.10%, respectively). The pore aspect ratio was also analysed to indicate their contribution to fracture as stress raisers. Elongated pores are considered the most detrimental because of stress concentrations induced by the sharp edges [48]. In the present specimens, the internal defects consist of only spherical pores (average aspect ratio of > 0.9) and elongated pores are absent. The distribution of porosity is relatively uniform among vertical and horizontal struts, and the spherical shape suggests that porosity is not a primary factor in dictating the location of first failure. Gorny [55] observed very large manufacturing induced pores up to 50 μm in the fracture surfaces close to nodes. In here, no pores have been detected in the fracture surfaces, see Supplementary Fig. 2.

Fig. 7 reports the volume rendered local thickness of the whole specimen prior to compression (a), of two horizontal struts, (b) and (c), and a vertical strut, (d); and at 0.2 remote strain in (e), (f) and (g), respectively. The horizontal struts were chosen at an equivalent position, where the stress distribution is expected to be identical in a

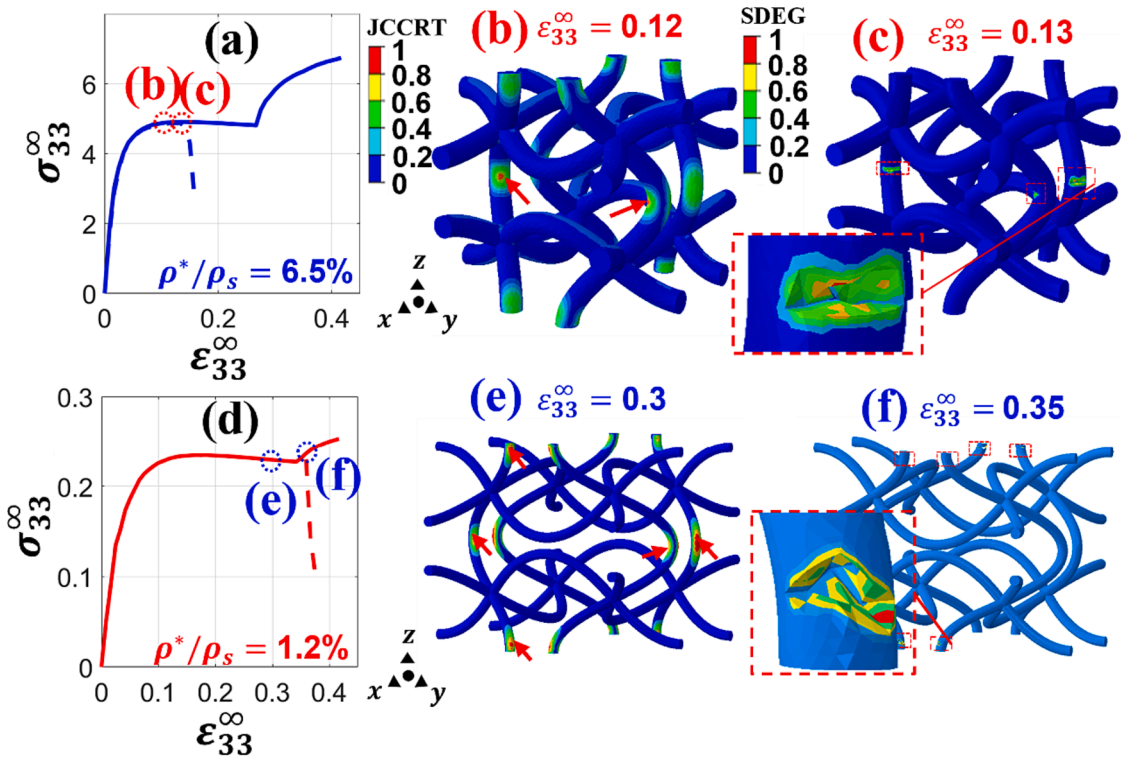

Fig. 5. Numerical compressive response of RVEs with relative density 6.5% (a)-(b)-(c) and 1.2% (d)-(e)-(f) with and without activated failure criteria. Solid and dotted lines are used to represent the response without and with the activation of the damage model, respectively. The distribution of the failure initiation criterion JCCRT and the stiffness degradation (SDEG) contour plots are shown for 6.5% relative density in (b) and (c) and for 1.2% in (e) and (f), respectively.

geometrically idealised structure. Before deformation, the maximum cross-sectional area reductions are 20.9% and 38.5% in horizontal struts (b) and (c), respectively, and of 13.4% in vertical strut (d). At macroscopic strain of 0.2, strut (b) sustains the load without fracture, by contrast, in strut (c) complete fracture had occurred due to the larger cross-sectional area reduction. In the vertical strut (d), complete failure occurred in the region with a 13.4% reduction in cross-sectional area. Hence, fracture appears to be caused by the expected localised stress at the plastic hinges of vertical and horizontal struts and occurs selectively in locations with reduced cross-sectional area due to manufacturing imperfections. Sercombe [38] reported a similar failure modality and location; failure preferentially initiates in the struts with high localised stress concentrations due to poor build quality. Similarly, for regular octet lattices, Liu [29] reported that variation in strut thickness significantly deteriorates the compressive strength. However, by tuning the thickness variation during the lattice manufacturing process it is possible to control the failure propagation and location. A detailed topological study is imperative to determine the geometrical improvements, as different lattice geometry, *e.g.,* Kagome and triangulated lattices [56], could have very different sensitivity to imperfections.

In other studies, nodes are the weakest points and stress concentrators for the initiation of failure. Novak [42] analysed the compressive properties of copper cubic chiral lattices manufactured by EPBF and reported initial failure at nodes. The discrepancy could be caused by the different quality of the printed part as a results of a different metal alloy powder and the higher strut diameter of 848 μm. As the defects are not quantified is difficult to make a more detailed comparison.

4. Discussion

4.1. Effective properties of chiral lattice

The dependence of mechanical properties of cellular architectures on relative density are typically provided through the Gibson - Ashby power scaling laws [21]. In lattices that deform by plastic yielding, the relevant elastic–plastic properties are the effective stiffness and yield strength, and the scaling laws are:

$$\frac{E^*}{E_S} = C_1 \left(\frac{\rho^*}{\rho_S}\right)^{N_1} \tag{4}$$

$$\frac{\sigma_Y^*}{\sigma_{Y,S}} = C_2 \left(\frac{\rho^*}{\rho_S}\right)^{N_2} \tag{5}$$

where E^*, σ_Y^*, ρ^* are the elastic stiffness, yield strength, and density of the lattice respectively. E_S, $\sigma_{Y,S}$, ρ_S are the analogous properties of the solid material and C_1, C_2, N_1, N_2 are non-dimensional fitting parameters. N_1 and N_2 are indicative of the deformation mechanisms (bending, stretching, buckling) and C_1 and C_2 are dependent on the topology of the architecture.

Fig. 8a-b summarise the scaling of elastic stiffness and yield strength with relative density for the cubic chiral lattice, for the unit cell RVE, the finite-sized specimen, and the experimental result. As in previous studies, the elastic modulus and yield stress increases with the increasing strut thickness, *i.e.,* relative density [25,57,58].

The effective stiffness of the cubic chiral unit cell scales with density through coefficients $C_1 = 0.32$ and exponent $N_1 = 1.95$. The exponent is in good agreement with idealised bending-dominated cellular structures, $N_1 = 2.0$[21]. Warmuth [44] reported $N_1 = 2.5$ from experimental tests on the finite-sized specimens of cubic chiral lattices. The higher exponent was attributed to irregular surfaces, roughness and porosity in the manufactured struts, which represent a deviation from the geometrically uniform assumption and are particularly relevant at small strut thickness. Transition in stiffness scaling has also been attributed to the slenderness ratio of the lattice beam struts, defined as $\lambda = \sqrt{A \bullet L/I}$ in which A is the cross sectional area, L the strut length and I the area moment of inertia. Meza [45] reported that in non-rigid tetrakaidecahedron lattices, the predicted scaling coefficient of $N_1 \sim 2$ is

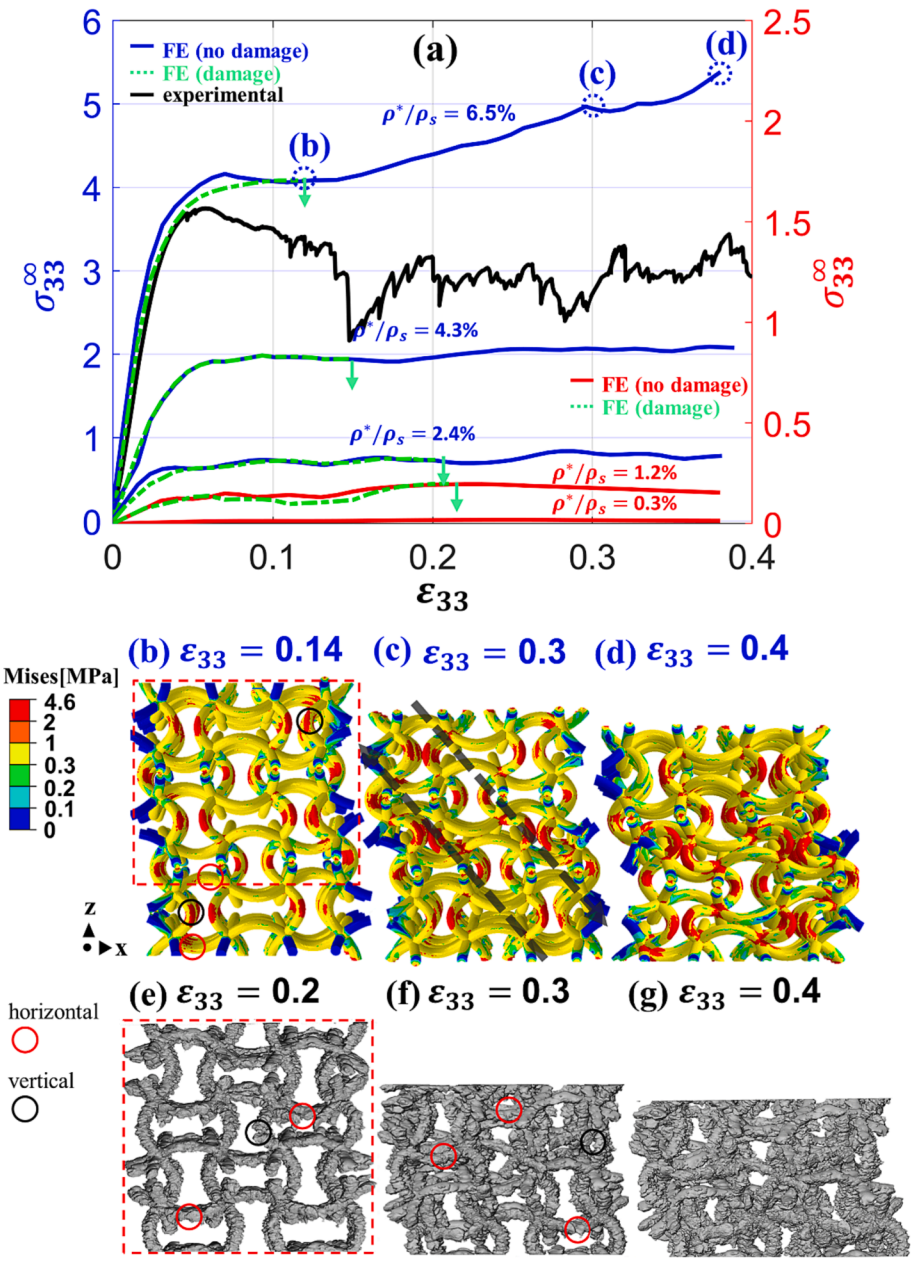

Fig. 6. Compressive response of (a) finite size numerical models, with and without damage criterion and experimental specimen; evolution of von Mises stress distribution in (b)-(d) the numerical model with relative density 6.5%, and (e)-(g) volume renderings of the experimental specimen at similar macroscopic strains. Fracture sites in horizontal and vertical struts of the numerical model and experimental specimen are red and black marked, respectively. (For interpretation of the references to colour in this figure legend, the reader is referred to the web version of this article.)

indeed achieved in the low-density regime, with strut slenderness ratio $\lambda > 7$ ($\rho^*/\rho_S \lesssim 7\%$); by contrast a different scaling law is attained in large density regimes due to the mixture of bending/stretching mechanisms in stockier struts, *e.g.*, $N_1 \approx 1$ when the slenderness ratio is $\lambda < 7$ ($\rho^*/\rho_S \gtrsim 7\%$). Here, the strut slenderness ratio is sufficiently large and the scaling law is linear in the range of relative density $0.3 \leq \rho^*/\rho_S \leq 6.5\%$.

The variation of yield strength with density scales with coefficient and exponent $C_2 = 0.99$ and $N_2 = 1.75$, respectively. These scaling values have not been reported in literature for this specific lattice architecture; but are characteristic of bending-dominated topologies [48]. Theoretical analyses of such topologies, simplified by slender beam assumptions, provide $N_2 = 1.5$[60], however when shearing and torsion of non-slender beams is taken into account, values in the range of $1.6 \leq N_2 \leq 1.9$ have been obtained experimentally for a range of rigid and non-rigid lattices [45], and re-entrant auxetic topologies [63].

In finite-sized specimens, the obtained scaling parameters are $C_1 = 0.33$, $C_2 = 0.87$, $N_1 = 1.97$, $N_2 = 1.75$. These results show good agreement with the scaling law of the unit cell RVE. Here, the results confirm that our selected finite-sized specimen could avoid edge effects, *i.e.*, the initial elastic–plastic response can adequately capture the analogous effective properties of the infinite lattice.

The compressive response of the EPBF AM-built specimen can be used to determine the influence of AM imperfections on mechanical properties, by comparison with the scaling laws of idealised models. The relative density of the experimental specimen is $\rho^*/\rho_S = 6.8\%$, the stiffness is $E^* = 111$ MPa (finite-sized specimens scaling relationship prediction $E^* = 190$ MPa), and the yield strength is $\sigma_Y^* = 3.2$ MPa (finite-sized specimens scaling relationship prediction $\sigma_Y^* = 3.4$ MPa). The stiffness of the experimental specimen is lower than that of the idealized model by a factor of 1.7 and yield stress is lower by a factor of 1.1. These results show that the presence of geometrical imperfections has an important effect on the reduction of the initial stiffness and, at larger compressive strains, has an influence in the determination of fracture location.

Fig. 8c summarises the change of the effective Poisson's ratios (ν_{ij}) with the range of relative densities $0.1\% \leq \rho^*/\rho_S \leq 6.5\%$. We examine

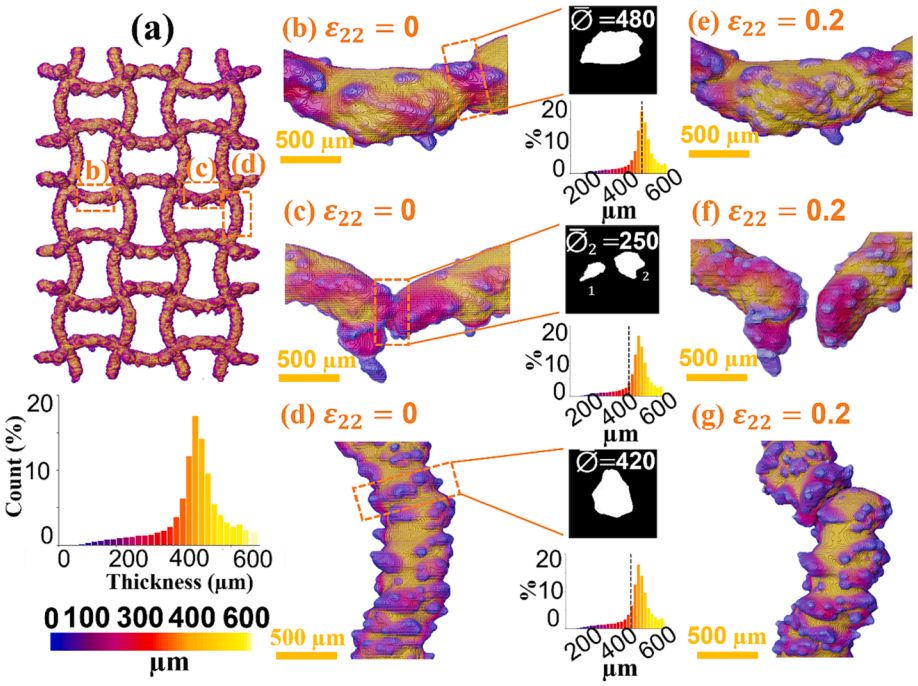

Fig. 7. Volume rendered local thickness of (a) the experimental lattice with (b)-(c), two horizontal struts highlighted with equivalent positions and (d) a vertical strut. The distribution of thickness and the cross-sectional areas are reported. For the same struts, (b)-(c)-(d) the distribution of thickness (e)-(f)-(g) is reported at 0.2 compression strain respectively.

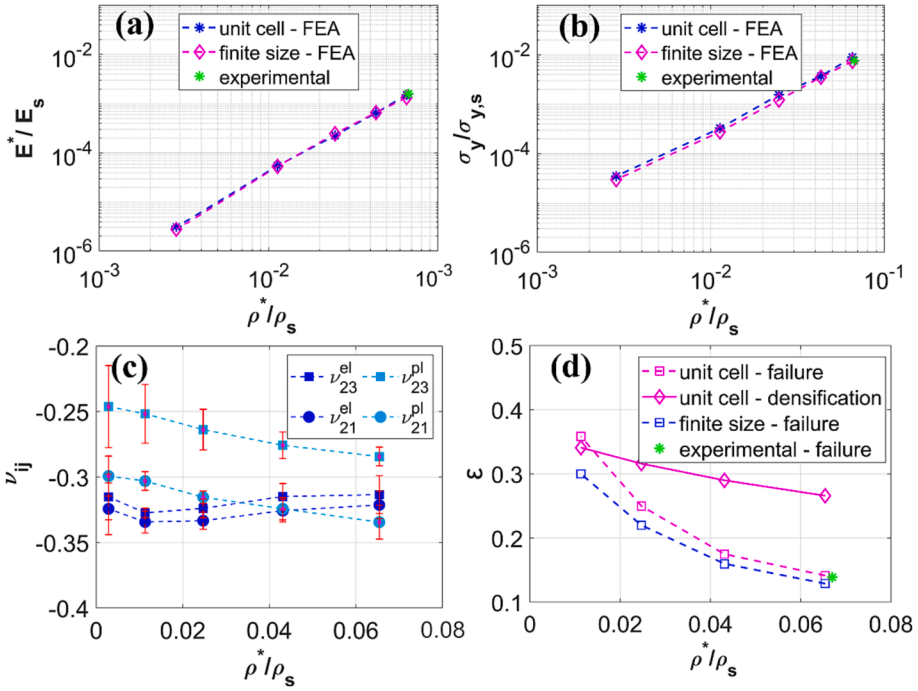

Fig. 8. Scaling relationships of the mechanical response of the cubic lattice with relative density: stiffness (a), yield strength (b), Poisson's ratios (d), and failure and densification strains (d).

the response in the elastic and plastic regimes separately, defined by the strain range $0 \leq \varepsilon \leq \varepsilon_P$(elastic) and $\varepsilon_P \leq \varepsilon \leq \varepsilon_D$ (plastic), in which ε_P is the 0.2% offset plastic strain and ε_D is the densification strain. There is considerable variation of Poisson's ratio with remote strain in the plastic range, see Fig. 4. To generalise our research findings, we report the mean and range of ν_{ij} in both regimes, in which the two characteristic Poisson's ratios of the lattice are represented by $\nu_{23} = \nu_{31} = \nu_{12}$ and $\nu_{21} = \nu_{32} = \nu_{13}$. In the elastic regime, there is minimal variation, both with relative density and directionality. Over the range of relative densities considered here, the mean and span of Poisson's ratios in this regime are $\nu_{21}^{el} = -0.327 \pm 0.005$ and $\nu_{23}^{el} = -0.319 \pm 0.005$, with a smaller value in ν_{21}^{el} indicating the preferential direction of contraction developed at larger strains. In contrast, in the plastic regime, we observe that the differences between the two sets of Poisson's ratios become larger than

in the elastic regime, due to the increased effect of preferential contraction, and both sets of Poisson's ratios decrease with the relative density. The latter can be explained by the relatively higher volume fraction of the material enclosed in the strut intersections (nodes) at higher densities, *e.g.,* from to $V_f = 0.054$ at $\rho^*/\rho_S = 0.3\%$ to $V_f = 0.22$ at $\rho^*/\rho_S = 6.5\%$. The higher volume fraction of joints increases the rotational stiffness of these areas, with the effect that at the same remote compressive strain, most deformation is localised in the plastic hinges, resulting in larger in-plane deflection and auxeticity.

The theoretical elastic Poisson's ratio of the ideal cubic chiral lattice of this geometry (mode 10 chirality) was first considered by Korner [14], who reported a value in the elastic regime $\nu^{el} = -0.4$, for a unit cell with amplitude $m = 1.4$ mm. The Poisson's ratios dependency with density in the large-deformation regimes has not previously been reported for this lattice. However, Mauko [61] reported the experimental response of a similar tetra-chiral lattice and observed that the Poisson's ratio decreases in magnitude at larger compressive strains; this response is also performed by the cubic chiral lattice in the low relative density regime ($\rho^*/\rho_S \leq 4.3\%$).

4.2. Influence of ductile failure on energy absorption

The fracture strains of the representative unit cell, finite-sized model, and experimental specimen are summarised in Fig. 8d. In the RVE, the ductile failure precedes densification in lattices with a relative density $\rho^*/\rho_S \geq 2.4\%$, while in finite-sized models and experimental specimen fracture occurs in individual struts, constrained by the compression plates or with pre-existing geometrical imperfections. From a design perspective, the most important consequence of failure in the plastic regime is the limitation in strain energy absorption per unit volume, defined as $W = \int_0^{\varepsilon_f} \sigma d\varepsilon$, where ε_f is the failure strain.

Fig. 9a-b show the variation of absorbed energy with peak stress, conventionally normalised by the stiffness of the solid, for the unit cell RVE and the finite size lattice. The "shoulder" in the energy curves of the RVE without ductile damage criteria, corresponds to the densification stress σ_D, and it indicates the maximum useful energy that can be absorbed by the lattice at the given plateau stress. The dashed line connecting these points for all the densities provides the relationship between the energy absorbed and peak stress for the optimum density [59], and is characteristic of the lattice geometry and collapse mechanism. In an idealised plastic foam, the relationship has the form:

$$\frac{W_{max}}{E_S} = \frac{\sigma_D}{E_S}\left(1 - C_3\left(\frac{\sigma_D}{E_S}\right)^{N_3}\right) \tag{6}$$

where the coefficients C_3 and N_3 depend on: the ratio of the material's yield strength to stiffness, the scaling of the lattice's yield strength with density (see *Equation (2)*, and the dependence of the densification strain on lattice relative density [58]. The current results produce $C_3 = 1.40$ and $N_3 = 0.06$. In the finite-sized lattice models, densification is delayed further due to the strut sliding permitted by the free surfaces of the specimen, thus extending the plateau regime, and the energy absorbed, past the maximum strain of 0.4 investigated here.

The energy absorption capacity of the finite size lattice is lowered by fracture, which can suddenly occur in a localised area and then propagates macroscopically. In the case of larger lattices samples, fracture propagates more gradually at macroscopic level. When large samples are approximated by RVE with PBCs, fracture starts in stress concentrators imposed by the boundary conditions, and geometric imperfections in the case of the finite-sized sample considered here. The effect of failure on the energy absorption curves is reported in Fig. 9 with green lines. The constants that describe the energy absorption envelope to failure are as follows: $C_3 = 1.65$ and $N_3 = 0.06$ for the RVE and $C_3 = 1.6$ and $N_3 = 0.06$ for the finite-size geometry, see Fig. 9b. There is reasonably good agreement in the energy envelopes of the RVE and finite size specimen,

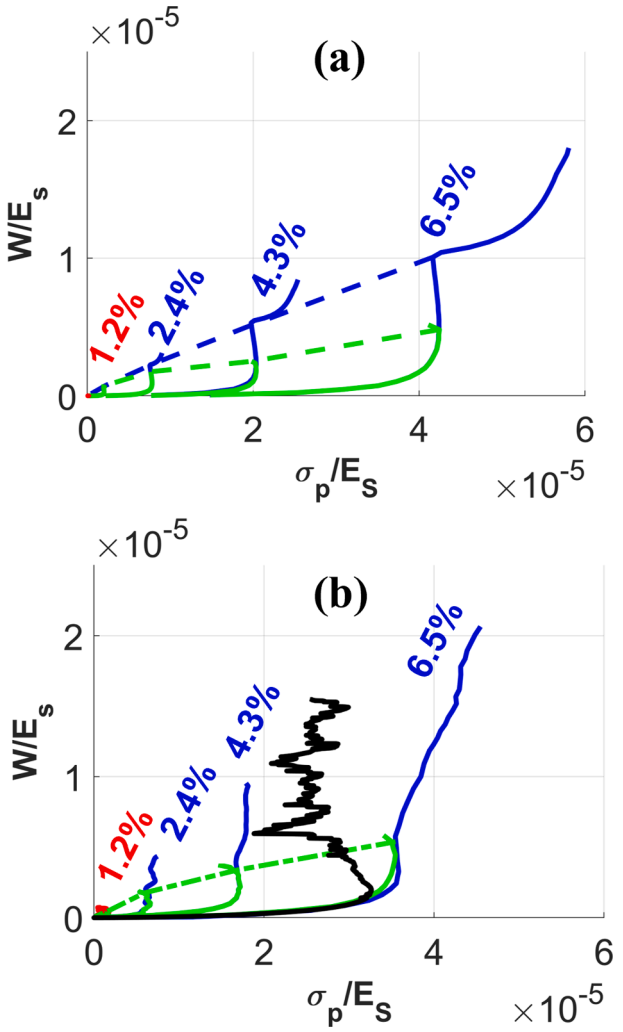

Fig. 9. Energy absorption diagram of the representative unit cell (a) and finite-sized specimen (b). The blue and green envelopes delineate the maximum normalised absorption energy values at densification and at failure, respectively. (For interpretation of the references to colour in this figure legend, the reader is referred to the web version of this article.)

and also, between the energy absorbed up to the first fracture of the experimental specimen and the energy envelope obtained by the numerical model. The initiation of ductile fracture can have a significant effect on the energy curves, reducing the energy absorption capacity of the larger density RVEs by a factor of 2. However, if subsequent gradual fracture, as observed in the experimental specimens, is acceptable in the design, the structure can continue absorbing external energy via the deformation of the remaining intact struts and progressive failure.

At large strains, the finite-sized cubic chiral lattice collapses through the localisation of deformation in a shear band at 45° to the loading axis. This has been previously observed in other compressive studies on stochastic foams [62], face centered cubic [25,38] and rhombic dodecahedron structures [63]. Topological modification of the lattice unit cell, can suppress the shear bands formation further enhancing the energy absorption capability [64].

5. Conclusions

In this work, a combination of numerical and experimental data gives insights on the deformation and failure mechanisms of auxetic cubic chiral lattices. Scaling relations are provided for stiffness and yield strength of finite and infinite size samples at varying relative densities

ranging from 0.3% to 6.5%, conforming to the power-law scaling relations of bending-dominated lattices.

In the elastic regime, the auxetic response of the lattice is isotropic and independent of relative density, with an average Poisson's ratio of −0.3. However, in the large plastic deformation (plateau) regime, the effective Poisson's ratio decreases in magnitude. Furthermore, in this regime, lattices with higher relative density exhibit larger in-plane auxeticity because the larger volume fraction at the joints increases their rotational stiffness.

Ductile fracture is delayed in lattices with low relative density, and below 1.2%, fracture occurs after densification. Our results confirm that the tensile/compressive stresses in the plastic hinges of vertical struts dictate the initiation and propagation of ductile failure. In the experimental specimens, additive manufacturing imperfections, principally the reduction in cross-sectional area of struts, dictate the location of failure. The geometrically idealised numerical model with a ductile failure criterion, can predict deformation and initiation of ductile failure with good accuracy. The presence of geometrical imperfection influences stiffness and fracture location predictions. The propagation of failure occurs gradually in the experimental specimens, showing good energy absorption capabilities up to large strain regions. At large strains, the finite-sized cubic chiral lattice collapses through the localisation of deformation in a shear band at 45° to the loading axis.

Declaration of Competing Interest

The authors declare that they have no known competing financial interests or personal relationships that could have appeared to influence the work reported in this paper.

Data availability

Data will be made available on request.

Acknowledgements

This research was supported by the European Space Agency (ESA) (through contract 4000132547 as part of ESA's Discovery Program); the EPSRC MAPP Future Manufacturing Hub (EP/P006566/1, www.mapp.ac.uk); the UK-EPSRC (grants EP/W031167/1, EP/W032147/1, EP/W037483/1, EP/W006774/1, EP/W003333/1, EP/V061798/1), the Royal Academy of Engineering (CiET1819/10); and the Research Complex at Harwell for use of facilities. The authors acknowledge financial support from the AMAZE project (Additive Manufacturing Aiming towards Zero Waste and Efficient Production of High-Tech Metal Products) funded by the seventh Framework Programme of the European Commission (contract FP7-2012-NMP-ICT-FoF-313781). The authors acknowledge Prof. Caroline Korner and the Erlangen Group for producing the samples.

Appendix A. Supplementary data

Supplementary data to this article can be found online at https://doi.org/10.1016/j.matdes.2023.112207.

References

[1] M. Qian, Metal powder for additive manufacturing, JOM 67 (3) (2015) 536–537.
[2] A. Joseph, V. Mahesh, D. Harursampath, On the application of additive manufacturing methods for auxetic structures: a review, Adv. Manuf. 9 (3) (2021) 342–368.
[3] J. Liu, X. Yao, Z. Wang, J. Ye, C. Luan, J. Fu, Y. He, A novel wavy non-uniform ligament chiral stent with J-shaped stress–strain behavior to mimic the native trachea, Bio-Design Manuf. 4 (4) (2021) 851–866.
[4] B. Xu, H. Fang, G. Cai, Y. Hou, S. Jiang, L. Lan, P. Liu, Space-reconfigurable reflector with auxetic lattice material, AIP Adv. 12 (1) (2022) 015101.
[5] P.R. Budarapu, Y.B. Sudhir Sastry, R. Natarajan, Design concepts of an aircraft wing: composite and morphing airfoil with auxetic structures, Front. Struct. Civ. Eng. 10 (4) (2016) 394–408.
[6] P. Sun, et al., Mechanics and extreme low-frequency band gaps of auxetic hexachiral acoustic metamaterial with internal resonant unit, Appl. Acoust. 200 (2022), 109046.
[7] W. Wu, W. Hu, G. Qian, H. Liao, X. Xu, F. Berto, Mechanical design and multifunctional applications of chiral mechanical metamaterials : a review, Mater. Des. 180 (June) (2019), 107950.
[8] C. Soyarslan, V. Blümer, S. Bargmann, Tunable auxeticity and elastomechanical symmetry in a class of very low density core-shell cubic crystals, Acta Mater. 177 (2019) 280–292.
[9] G.S..S., C.I.R.L.J. Gibson, M.F. Ashby, The Mechanics of Two-Dimensional Cellular Materials, vol. 382, no. 1782, pp. 25–42, 1982.
[10] Z.-P. Wang, L.H. Poh, J. Dirrenberger, Y. Zhu, S. Forest, Isogeometric shape optimization of smoothed petal auxetic structures via computational periodic homogenization, Comput. Methods Appl. Mech. Engrg. 323 (2017) 250–271.
[11] N. R. Æ. A. A. Æ. K. L. Alderson, Interlocking hexagons model for auxetic behaviour, no. May, pp. 7433–7445, 2007.
[12] X. Peng, C. Soyarslan, S. Bargmann, Phase contrast mediated switch of auxetic mechanism in composites of infilled re-entrant honeycomb microstructures, Extrem. Mech. Lett. 35 (2020), 100641.
[14] C. Korner, Y. Liebold-Ribeiro, A systematic approach to identify cellular auxetic materials, Smart Mater. Struct. 24 (2) (2015).
[15] Y.-L. Wei, Q.-S. Yang, X. Liu, R. Tao, A novel 3D anti-tetrachiral structure with negative Poisson's ratio, Smart Mater. Struct. 29 (8) (2020) 085003.
[16] J. Zhang, G. Lu, Z. You, Large deformation and energy absorption of additively manufactured auxetic materials and structures: a review, Compos. Part B 201 (August) (2020), 108340.
[17] Q. Wang, Z. Yang, Z. Lu, X. Li, Mechanical responses of 3D cross-chiral auxetic materials under uniaxial compression, Mater. Des. 186 (2020), 108226.
[18] R. Hamzehei *et al.*, Parrot Beak-Inspired Metamaterials with Friction and Interlocking Mechanisms 3D / 4D Printed in Micro and Macro Scales for Supreme Energy Absorption / Dissipation, vol. 2201842, 2023.
[19] R. Hamzehei, A. Serjouei, N. Wu, A. Zolfagharian, M. Bodaghi, 4D metamaterials with Zero Poisson ' s ratio, shape recovery, and energy absorption features, Adv. Eng. Mater. 2200656 (24) (2022).
[20] M. Mazur, M. Leary, S. Sun, M. Vcelka, D. Shidid, M. Brandt, Deformation and failure behaviour of Ti-6Al-4V lattice structures manufactured by selective laser melting (SLM), Int. J. Adv. Manuf. Technol. 84 (5–8) (2016) 1391–1411.
[21] M.F.A.L.J. Gibson, M.F. Ashby, A. Michael, Cellular Materials: Structure and Properties, 2nd ed., Cambridge University Press, 1999.
[22] P.R. Onck, E.W. Andrews, L.J. Gibson, Size effects in ductile cellular solids. Part I: Modeling, Int. J. Mech. Sci. 43 (3) (2001) 681–699.
[23] S.J.N. Morrish, M. Pedersen, K.F.W. Wong, I. Todd, R. Goodall, Size effects in compression in Electron Beam Melted Ti6Al4V diamond structure lattices, Mater. Lett. 190 (2017) 138–142.
[24] I. Echeta, X. Feng, B. Dutton, R. Leach, S. Piano, Review of defects in lattice structures manufactured by powder bed fusion, Int. J. Adv. Manuf. Technol. 106 (5–6) (2020) 2649–2668.
[25] Y. Amani, S. Dancette, P. Delroisse, A. Simar, E. Maire, Compression behavior of lattice structures produced by selective laser melting : X-ray tomography based experimental and finite element approaches, Acta Mater. 159 (2018) 395–407.
[26] C. Iantaffi, et al., Oxidation induced mechanisms during directed energy deposition additive manufactured titanium alloy builds, Addit. Manuf. Lett. 1 (October) (2021), 100022.
[27] C.L.A. Leung, R. Tosi, E. Muzangaza, S. Nonni, P.J. Withers, P.D. Lee, Effect of preheating on the thermal, microstructural and mechanical properties of selective electron beam melted Ti-6Al-4V components, Mater. Des. 174 (2019), 107792.
[28] A. Safdar, H. Z. He, L. Wei, A. Ab, L. E. C. De Paz, Effect of process parameters settings and thickness on surface roughness of EBM produced Ti-6Al-4V, vol. 5, no. December 2011, pp. 401–408, 2012.
[29] L. Liu, P. Kamm, F. García-Moreno, J. Banhart, D. Pasini, Elastic and failure response of imperfect three-dimensional metallic lattices: the role of geometric defects induced by Selective Laser Melting, J. Mech. Phys. Solids 107 (2017) 160–184.
[30] S. Van Bael, G. Kerckhofs, M. Moesen, G. Pyka, J. Schrooten, J.P. Kruth, Micro-CT-based improvement of geometrical and mechanical controllability of selective laser melted Ti6Al4V porous structures, Mater. Sci. Eng. A 528 (24) (2011) 7423–7431.
[31] S. Arabnejad, R.B. Johnston, J. Ann, B. Singh, M. Tanzer, D. Pasini, High-strength porous biomaterials for bone replacement: a strategy to assess the interplay between cell morphology, mechanical properties, bone ingrowth and manufacturing constraints, Acta Biomater. 30 (2016) 345–356.
[32] A.T. Sidambe, Three dimensional surface topography characterization of the electron beam melted Ti6Al4V, Met. Powder Rep. 72 (3) (2017) 200–205.
[33] A. Ataee, Y. Li, D. Fraser, G. Song, C. Wen, Anisotropic Ti-6Al-4V gyroid scaffolds manufactured by electron beam melting (EBM) for bone implant applications, Mater. Des. 137 (2018) 345–354.
[34] A. El Elmi, D. Melancon, M. Asgari, L.u. Liu, D. Pasini, Experimental and numerical investigation of selective laser melting-induced defects in Ti-6Al-4V octet truss lattice material: The role of material microstructure and morphological variations, J. Mater. Res. 35 (15) (2020) 1900–1912.
[35] M. Gavazzoni, L. Boniotti, S. Foletti, Influence of specimen size on the mechanical properties of microlattices obtained by selective laser melting, Proc. Inst. Mech. Eng. Part C J. Mech. Eng. Sci. 235 (10) (2021) 1774–1787.

[36] C. Yan, L. Hao, A. Hussein, P. Young, D. Raymont, Advanced lightweight 316L stainless steel cellular lattice structures fabricated via selective laser melting, Mater. Des. 55 (2014) 533–541.
[37] R. Noroozi, F. Tatar, A. Zolfagharian, and R. Brighenti, Additively Manufactured Multi-Morphology Bone-like Porous Scaffolds : Experiments and Micro-Computed Tomography-Based Finite Element Modeling Approaches, pp. 40–53, 2022.
[38] T.B. Sercombe, X. Xu, V.J. Challis, R. Green, S. Yue, Z. Zhang, P.D. Lee, Failure modes in high strength and stiffness to weight scaffolds produced by Selective Laser Melting, Mater. Des. 67 (2015) 501–508.
[39] H.D. Carlton, J. Lind, M.C. Messner, N.A. Volkoff-Shoemaker, H.S. Barnard, N. R. Barton, M. Kumar, Mapping local deformation behavior in single cell metal lattice structures, Acta Mater. 129 (2017) 239–250.
[40] A. Alderson, K.L. Alderson, Auxetic materials, Proc. Inst. Mech. Eng. Part G J. Aerosp. Eng. 221 (4) (2007) 565–575.
[41] W. Liu, N. Wang, T. Luo, Z. Lin, In-plane dynamic crushing of re-entrant auxetic cellular structure, Mater. Des. 100 (2016) 84–91.
[42] N. Novak, L. Starčevič, M. Vesenjak, Z. Ren, Blast response study of the sandwich composite panels with 3D chiral auxetic core, Compos. Struct. 210 (October 2018) (2019) 167–178.
[43] N. Novak, M. Vesenjak, S. Tanaka, K. Hokamoto, Z. Ren, Compressive behaviour of chiral auxetic cellular structures at different strain rates, Int. J. Impact Eng. 141 (2020) 103566.
[44] F. Warmuth, F. Osmanlic, L. Adler, M.A. Lodes, C. Körner, Fabrication and characterisation of a fully auxetic 3D lattice structure via selective electron beam melting, Smart Mater. Struct. 26 (2) (2017).
[45] L.R. Meza, G.P. Phlipot, C.M. Portela, A. Maggi, L.C. Montemayor, A. Comella, D. M. Kochmann, J.R. Greer, Reexamining the mechanical property space of three-dimensional lattice architectures, Acta Mater. 140 (2017) 424–432.
[46] A. Du Plessis, D. Kouprianoff, I. Yadroitsava, and I. Yadroitsev, Mechanical Properties and In Situ Deformation Imaging of Microlattices Manufactured by Laser Based Powder Bed Fusion, 2018.
[47] G.R. Johnson, W.H. Cook, A Computational constitutive model and data for metals subjected to large strain, high strain rates and high pressures, Seventh Int. Symp. Ballist. (1983) 541–547.
[48] M. Wang, H.Q. Li, D.J. Lou, C.X. Qin, J. Jiang, X.Y. Fang, Y.B. Guo, Microstructure anisotropy and its implication in mechanical properties of biomedical titanium alloy processed by electron beam melting, Mater. Sci. Eng. A 743 (2019) 123–137.
[49] Y. Zhang, J.C. Outeiro, T. Mabrouki, On the selection of Johnson-Cook constitutive model parameters for Ti-6Al-4V using three types of numerical models of orthogonal cutting, Procedia CIRP 31 (2015) 112–117.
[50] A.R. Melro, P.P. Camanho, F.M. Andrade Pires, S.T. Pinho, Micromechanical analysis of polymer composites reinforced by unidirectional fibres: Part II-Micromechanical analyses, Int. J. Solids Struct. 50 (11–12) (2013) 1906–1915.
[51] A. Mishra, Analysis of friction and wear of titanium alloys, Int. J. Mech. Eng. Robot. Res. 3 (3) (2014).
[52] W. Liu, et al., Study of pore defect and mechanical properties in selective laser melted Ti6Al4V alloy based on X-ray computed tomography, Mater. Sci. Eng. A 797 (August) (2020), 139981.
[53] L. Sinclair, et al., In situ radiographic and ex situ tomographic analysis of pore interactions during multilayer builds in laser powder bed fusion, Addit. Manuf. 36 (July) (2020), 101512.
[54] T. Hildebrand, P. Rüegsegger, A new method for the model-independent assessment of thickness in three-dimensional images, J. Microsc. 185 (1) (1997) 67–75.
[55] B. Gorny, T. Niendorf, J. Lackmann, M. Thoene, T. Troester, H.J. Maier, In situ characterization of the deformation and failure behavior of non-stochastic porous structures processed by selective laser melting, Mater. Sci. Eng. A 528 (27) (2011) 7962–7967.
[56] D. D. Symons, N. A. Fleck, The Imperfection Sensitivity of Isotropic Two-Dimensional Elastic Lattices, vol. 75, no. September, pp. 1–8, 2008.
[57] J. Parthasarathy, B. Starly, S. Raman, A. Christensen, Mechanical evaluation of porous titanium (Ti6Al4V) structures with electron beam melting (EBM), J. Mech. Behav. Biomed. Mater. 3 (3) (2010) 249–259.
[58] T. G. Nieh, K. Higashi, J. Wadsworth, Effect of cell morphology on the compressive properties of open-cell aluminum foams, vol. 283, pp. 105–110, 2000.
[59] N.A. Fleck, V.S. Deshpande, M.F. Ashby, Micro-architectured materials: Past, present and future, Proc. R. Soc. A Math. Phys. Eng. Sci. 466 (2121) (2010) 2495–2516.
[60] L. Yang, O. Harrysson, H. West, D. Cormier, Compressive properties of Ti-6Al-4V auxetic mesh structures made by electron beam melting, Acta Mater. 60 (8) (2012) 3370–3379.
[61] A. Mauko, T. Fíla, J. Falta, P. Koudelka, V. Rada, M. Neuhäuserová, P. Zlámal, M. Vesenjak, O. Jiroušek, Z. Ren, Dynamic deformation behaviour of chiral auxetic lattices at low and high strain-rates, Metals (Basel) 11 (1) (2021) 52.
[62] X. Y. Cheng *et al.*, Compression deformation behavior of Ti – 6Al – 4V alloy with cellular structures fabricated by electron beam melting, vol. 16, pp. 153–162, 2012.
[63] L. Xiao, W. Song, C. Wang, H. Liu, H. Tang, J. Wang, Mechanical behavior of open-cell rhombic dodecahedron Ti-6Al-4V lattice structure, Mater. Sci. Eng. A 640 (2015) 375–384.
[64] O. Al-ketan, R. Rowshan, R.K.A. Al-rub, Topology-mechanical property relationship of 3D printed strut, skeletal, and sheet based periodic metallic cellular materials, Addit. Manuf. 19 (2018) 167–183.

Further reading

[13] C. W. Smith, J. N. Grima, K. E. Evans, A novel mechanism for generating auxetic behaviour in reticulated foams: missing RIB foam model, 48, 4349–4356, 2000.